Structure and assembly of the mouse ASC inflammasome by combined NMR spectroscopy and cryo-electron microscopy

Lorenzo Sborgi[a,1], Francesco Ravotti[b,1], Venkata P. Dandey[c,1], Mathias S. Dick[a], Adam Mazur[a,d], Sina Reckel[a,2], Mohamed Chami[c], Sebastian Scherer[c], Matthias Huber[b], Anja Böckmann[e], Edward H. Egelman[f], Henning Stahlberg[c], Petr Broz[a,3], Beat H. Meier[b,3], and Sebastian Hiller[a,3]

[a]Biozentrum, University of Basel, 4056 Basel, Switzerland; [b]Physical Chemistry, Swiss Federal Institute of Technology in Zurich, 8093 Zurich, Switzerland; [c]Center for Cellular Imaging and NanoAnalytics, Biozentrum, University of Basel, 4058 Basel, Switzerland; [d]Research IT, Biozentrum, University of Basel, 4056 Basel, Switzerland; [e]Institute for the Biology and Chemistry of Proteins, 69367 Lyon, France; and [f]Department of Biochemistry and Molecular Genetics, University of Virginia, Charlottesville, VA 22908

Edited by Gerhard Wagner, Harvard Medical School, Boston, MA, and approved September 24, 2015 (received for review April 17, 2015)

Inflammasomes are multiprotein complexes that control the innate immune response by activating caspase-1, thus promoting the secretion of cytokines in response to invading pathogens and endogenous triggers. Assembly of inflammasomes is induced by activation of a receptor protein. Many inflammasome receptors require the adapter protein ASC [apoptosis-associated speck-like protein containing a caspase-recruitment domain (CARD)], which consists of two domains, the N-terminal pyrin domain (PYD) and the C-terminal CARD. Upon activation, ASC forms large oligomeric filaments, which facilitate procaspase-1 recruitment. Here, we characterize the structure and filament formation of mouse ASC in vitro at atomic resolution. Information from cryo-electron microscopy and solid-state NMR spectroscopy is combined in a single structure calculation to obtain the atomic-resolution structure of the ASC filament. Perturbations of NMR resonances upon filament formation monitor the specific binding interfaces of ASC-PYD association. Importantly, NMR experiments show the rigidity of the PYD forming the core of the filament as well as the high mobility of the CARD relative to this core. The findings are validated by structure-based mutagenesis experiments in cultured macrophages. The 3D structure of the mouse ASC-PYD filament is highly similar to the recently determined human ASC-PYD filament, suggesting evolutionary conservation of ASC-dependent inflammasome mechanisms.

inflammation | protein structure | protein filament | ASC speck | innate immune response

The innate immune system rapidly detects and responds to different types of pathogen- and danger-associated molecular patterns (PAMPs and DAMPs, respectively) at minimal concentrations via specific, germline-encoded pattern-recognition receptors (PRRs) (1–3). A subset of cytosolic PRRs respond to PAMPs and DAMPs by initiating the assembly of cytosolic macromolecular inflammasome complexes (4–6). Inflammasome assembly leads to the activation of caspase-1, the proteolytic maturation of interleukins, and the induction of pyroptosis. The correct assembly of inflammasome complexes is critical, and malfunctions are related to major human diseases including cancer and autoimmune syndromes (4, 7). Inflammasome signaling initiates with the activation of dedicated sensor proteins, such as the NOD-like receptor (NLR) family, through mechanisms that still are poorly understood (2, 4). The typical domain architecture of NLRs is tripartite, including an N-terminal effector domain (8). Based on the type of effector domain, which can be pyrin domains (PYDs), caspase-recruitment domains (CARDs), or baculovirus inhibitor of apoptosis (IAP) repeat (BIR) domains, NLRs are classified as NLRPs, NLRCs, or NLRBs, respectively (9). In the initial reaction step upon recognition of the specific molecular pattern, the receptor self-associates (Fig. 1*A*). Because death domains interact in a homotypic fashion, NLRCs can activate procaspase-1, which features a CARD, directly. In contrast, NLRPs require the recruitment of the bipartite adaptor protein ASC (apoptosis-associated speck-like protein containing a CARD) as an intermediate signaling step. ASC interacts with the receptor via its N-terminal PYD and activates procaspase-1 with its C-terminal CARD. Importantly, the interaction with the receptor is not stoichiometric, but ASC oligomerizes in vivo to a micrometer-sized assembly, the ASC speck (Fig. 1 *A* and *B*) (10). Procaspase-1 is recruited to the speck, resulting in its autoprocessing and the formation of the catalytically active heterotetramer of cleaved p10 and p20 subunits.

Given its central role in NLRP inflammasomes, a description of ASC structure and dynamics in its soluble and filamentous form is crucial to understand inflammation processes at the atomic level. NMR spectroscopy is the method of choice for the structural and functional characterization of PYDs that are

Significance

Invading pathogens and other danger-associated signals are recognized by the innate immune system. Subsequently, the eukaryotic protein ASC [apoptosis-associated speck-like protein containing a caspase-recruitment domain (CARD)] assembles to long filaments, which might serve to amplify the signal and activate an inflammatory response. We have determined the structure of the mouse ASC filament at atomic resolution. The pyrin domain of ASC forms the helical filament core, and the CARD, thus far elusive to experimental observation, is flexibly unfolded on the filament periphery. The integration of data from two structural methods, cryo-electron microscopy and solid-state NMR spectroscopy, opens perspectives for structural studies of inflammasomes and related molecular assemblies.

Author contributions: L.S., F.R., A.M., A.B., H.S., P.B., B.H.M., and S.H. designed research; L.S., F.R., V.P.D., M.S.D., A.M., S.R., M.C., S.S., and M.H. performed research; L.S., F.R., V.P.D., M.S.D., A.M., S.R., M.C., S.S., A.B., E.H.E., H.S., P.B., B.H.M., and S.H. analyzed data; and L.S., F.R., M.S.D., A.M., A.B., E.H.E., H.S., P.B., B.H.M., and S.H. wrote the paper.

The authors declare no conflict of interest.

This article is a PNAS Direct Submission.

Freely available online through the PNAS open access option.

Data deposition: The density map from cryo-EM data was deposited in the Electron Microscopy Data Bank (accession code EMD-2971). The atomic coordinates of the ASC PYD filament (model 3) were deposited in the Protein Data Bank (PDB ID code 2N1F). Chemical shifts of the soluble and filament form of mouse ASC-PYD were submitted to the Biological Magnetic Resonance Bank (accession codes 25561 and 26550, respectively).

[1]L.S., F.R., and V.P.D. contributed equally to this work.

[2]Present address: School of Life Sciences, Swiss Federal Institute of Technology in Lausanne, 1015 Lausanne, Switzerland.

[3]To whom correspondence may be addressed. Email: petr.broz@unibas.ch, beme@ethz.ch, or sebastian.hiller@unibas.ch.

This article contains supporting information online at www.pnas.org/lookup/suppl/doi:10.1073/pnas.1507579112/-/DCSupplemental.

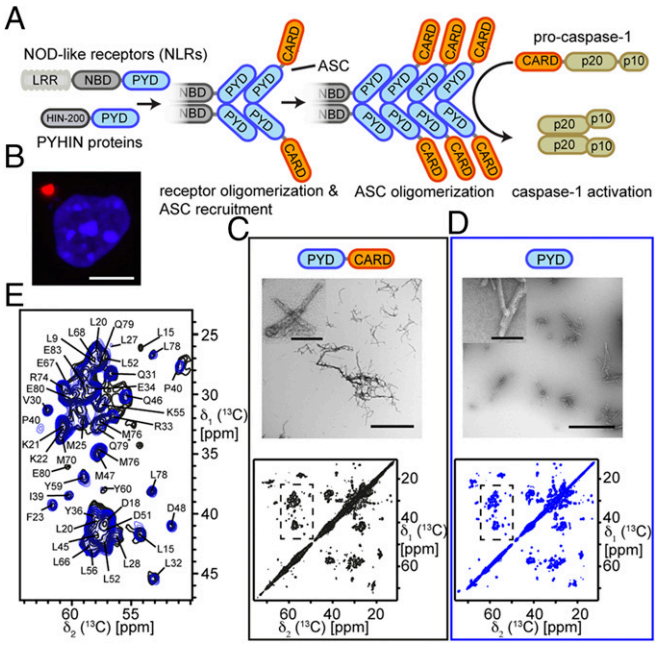

Fig. 1. Structural determinants of ASC filament formation. (*A*) Schematic representation of ASC-mediated inflammasome assembly and caspase-1 activation. Detection of specific molecular patterns by NLR or pyrin and HIN domain-containing protein (PYHIN) family members results in their activation and oligomerization. Activated receptors recruit the inflammasome adaptor ASC, which in turn oligomerizes to ASC filaments. The effector protease caspase-1 is activated by this complex. LRR, leucine-rich repeat. (*B*) Endogenous ASC specks in immortalized murine macrophages stained with antibodies for ASC (red) appear as large, macromolecular complexes. Nuclei are stained blue. (Scale bar, 5 μm.) (*C* and *D*) Characterization of filaments from ASC-FL (*C*, black) and ASC-PYD (*D*, blue) reconstituted in vitro. (*Upper*) EM images of negatively stained preparations of ASC filaments. (Scale bars, 1 μm; 100 nm in *Insets*). (*Lower*) 2D [^{13}C,^{13}C]-DARR solid-state NMR spectra of [U-^{13}C]-labeled filaments (mixing time 20 ms). The spectra were recorded on an 850-MHz spectrometer at 17 kHz MAS. (*E*) Superimposition of a selected region of the 2D [^{13}C,^{13}C]-DARR spectra shown in *C* and *D*. Sequence-specific resonance assignments are indicated.

difficult to crystallize (11–13). In particular, the solution structures of isolated human ASC pyrin domain (ASC-PYD) and ASC full-length protein (ASC-FL) have been determined, showing that the PYD and the CARD, connected by a flexible linker, tumble independently in solution (14, 15). A suitable method for the structural characterization of the insoluble ASC aggregates that form at physiological pH conditions is cryo-EM, which recently has provided the first structure of an ASC-PYD filament at near-atomic resolution (16). Filaments of human ASC-PYD feature a helical arrangement along well-defined molecular interfaces, in agreement with other molecular assemblies of death domains (16–18). An alternative method to determine structures of insoluble protein assemblies at atomic resolution is solid-state NMR spectroscopy under magic-angle-spinning (MAS) conditions (19–22). Cryo-EM density maps do not recover disordered or dynamic polypeptide segments, but solid-state NMR spectroscopy renders data from both the rigid and dynamic parts of a molecular assembly. The two techniques thus can provide complementary information. Structural studies of inflammasomes from different vertebrates remain of great interest because of the extensive diversification of inflammasome signaling pathways among species.

Here, we combine data from solid-state NMR spectroscopy and cryo-EM to determine the atomic-resolution structure of mouse ASC filaments formed by the PYDs via helical stacking along well-defined interfaces. Additional solid-state NMR measurements address the dynamic CARD as part of the ASC-FL filament. A comparison of chemical shifts reveals conformational changes upon filament formation. Structure-guided mutagenesis in living cells confirms the network of interactions that are essential for the integrity of the filament and thus ASC-dependent inflammasome signaling.

Results

Reconstitution and Characterization of ASC Filaments in Vitro. The mouse ASC-FL and ASC-PYD were soluble at low pH or in chaotropic solution and showed a high propensity for assembling into filaments at physiological pH conditions. Negatively stained preparations visualized by EM showed that oligomerization leads to the formation of long, well-defined filaments, with typical lengths in the range of 500–2,000 nm (Fig. 1 *C* and *D*). The filaments were organized in larger aggregates of variable size, with the ASC-FL filaments branching more frequently than the ASC-PYD filaments. In general, the atomic structure of filaments depends on the assembly conditions in vivo and in vitro, and polymorphism is common in some systems (23, 24). To characterize the sample homogeneity in our preparations, we used solid-state NMR spectroscopy, which is highly sensitive to even small changes in the local molecular conformation (23). A 2D dipolar-assisted rotational resonance (DARR) [^{13}C,^{13}C]-correlation spectrum as well as an NCA correlation spectrum of the filament of the isolated PYD showed narrow cross-peaks, with typical carbon line widths of about 0.5 ppm (Fig. 1 *D* and *E* and Fig. S1). The observation of a single set of peaks—one per carbon or nitrogen atom—is a strong indication of a homogeneous preparation and the absence of polymorphism. Notably, the observation of a single set of resonances also indicates that all monomers in the filament are symmetry-equivalent. We repeated the same experiments on the filament of ASC-FL under the same conditions and observed highly similar DARR and NCA spectra (Fig. 1 *C* and *E* and Fig. S1). The two pairs of spectra feature a complete set of correlation cross-peaks at the same positions, indicating that the CARD is essentially invisible in the spectrum of ASC-FL and that the observable PYD adopts the same structure in both types of filament. The ASC-PYD alone thus forms the scaffold of the ASC-FL filament, whereas the CARD is not strictly required for the filament core and does also not perturb the PYD filament conformation. The absence of additional strong signals in the full-length protein relative to the PYD shows that the CARD is flexible relative to the filament core. Consistently, although mouse ASC-PYD filaments feature a smooth surface in negative-stained EM, filaments formed by mouse ASC-FL have a rough surface, possibly because the ASC-CARD is exposed outside the ASC filament (Fig. 1 *C* and *D*). These data directly indicate that the two domains of mouse ASC, which in human ASC have been shown to tumble independently in solution (14), also are independent in the filament form.

Cryo-EM of the ASC-PYD Filament. Based on the observation that the ASC-PYD is the minimal structural requirement for filament formation, we studied the structure of filaments of the mouse ASC-PYD without the CARD. Optimization of the filament formation protocol by observation with cryo-EM showed that these filaments are well-ordered (Fig. S2). Image collection was done manually on an FEI Titan Krios transmission electron microscope using a Gatan K2 Summit direct electron detector. Recorded image series were automatically drift-corrected and averaged using the 2dx_automator (25), employing MOTIONCORR (26). The averaged power spectrum of multiple individual segments of filaments from these cryo-EM images shows a clear meridional reflection at 1/14.2 Å^{-1}, corresponding to the reciprocal of the axial rise. Image processing with the Iterative Helical Real Space Reconstruction (IHRSR) method (27) yielded a final electron density map at a resolution of ~4.0–4.5 Å (Fig. 2*A*). The ASC-PYD filament is a hollow helical fiber with inner and outer diameters of 20 Å and 90 Å, respectively. The polar filament has C3 point group symmetry with 53° right-handed rotation and a 14.2-Å axial rise per subunit.

Solid-State NMR of the Mouse ASC-PYD Filament. For the resonance assignment, we recorded a set of correlation experiments on uniformly ^{13}C- and ^{15}N-labeled filaments under MAS conditions

(28). The spectra were well resolved and allowed sequence-specific resonance assignments of the backbone and amino acid side chains, as detailed in ref. 29 (Fig. 2 *B* and *C*). The backbone assignment was complete for residues 4–84, and in this segment most of the side-chain carbon atoms were assigned also. The secondary chemical shifts allowed a direct determination of the location of secondary-structure elements. Mouse ASC-PYD in its filament form features six α-helices at positions 3–14, 17–29, 41–46, 49–59, 62–76, and 80–84 (Fig. 2*D*). The last helix presumably extends until residue 89, but resonances that could correspond to the segment 85–89 were not found in any of the spectra. Because an INEPT (insensitive nuclei enhanced by polarized transfer)-based spectrum of the ASC-PYD filaments did not show resonances, we assume that these four residues feature millisecond dynamics, leading to line broadening below the level of detection, a common feature of terminal residues even in microcrystalline proteins (30).

Calculation of the Structure of the Mouse ASC-PYD Filament. The cryo-EM density map of the ASC-PYD filament was combined with solid-state NMR data toward a joined structure calculation, which proceeded in three steps (Fig. 2*E*). Model 1 of the ASC-PYD filament monomer is based on the EM electron density map and on the location of the six α-helical segments in the amino acid sequence, as determined from solid-state NMR secondary chemical shifts. It was built by placing the helices interactively into the cryo-EM density map using Coot (31) and connecting them as indicated by electron density. Because some of the side chains were well resolved in the electron density map, matching them allowed a tentative rotational orientation. The full-filament coordinates were created from this monomer by application of the helical symmetry (C3, 53° rotation, 14.2-Å rise). The resulting model 1 was refined further using the X-PLOR-NIH program (32) under continuous symmetry enforcement, using the cryo-EM structure factors (the Fourier transform of the density map) as restraints, as well as the TALOS+ dihedral angles from solid-state NMR chemical shifts for a total of 70 residues and *i*,*i*+4 backbone hydrogen-bond restraints for residues in α-helical secondary structure (see above). The resulting model 2 shows a well-defined backbone structure, as indicated by a backbone rmsd of 0.23 Å and an overall heavy atom rmsd of 0.94 Å for the conformer bundle. Model 2 is cross-validated by a set of spectrally unambiguous cross-peaks in 2D [^{13}C,^{13}C]-CHHC and [^{13}C,^{13}C]-proton assisted recoupling (PAR) solid-state NMR experiments, which are all in agreement with the 3D structure (Fig. S3*A* and Table S1).

In an attempt to improve side-chain orientations, we used further NMR distance restraints from 2D [^{13}C,^{13}C]-CHHC and [^{13}C,^{13}C]-PAR spectra. The spectra were peak-picked automatically by Sparky (33) and assigned to 674 atom pairs with the CANDID algorithm (34) using the 3D structure information of model 2 as input (Fig. S3*B*). A structure calculation with X-PLOR-NIH (32) under symmetry enforcement yielded model 3, using as input the cryo-EM–derived structure factors, TALOS+-derived dihedral angle restraints, and the 674 ambiguous NMR distance restraints but no hydrogen-bond restraints. In model 3, the ensemble of the 10 lowest energy conformers of the ASC-PYD filament featured a backbone rmsd of 0.17 Å and an overall heavy atom rmsd of 0.63 Å (Fig. 2 *F*–*I*, Table S2, and Movies S1 and S2). Because all data, including the EM map, were treated with strict symmetry enforcement, these values are equally representative for the individual monomer subunits.

A comparison of model 3 with model 1 showed significant improvements. The models differ by backbone and all heavy atom rmsds of 0.84 Å and 1.04 Å, respectively. The comparison of model 3 with model 2 showed only small differences overall (backbone and all heavy atom rmsds of 0.27 Å and 0.33 Å, respectively). Visual inspection showed that the improvement is not uniform but that a number of side-chain orientations were

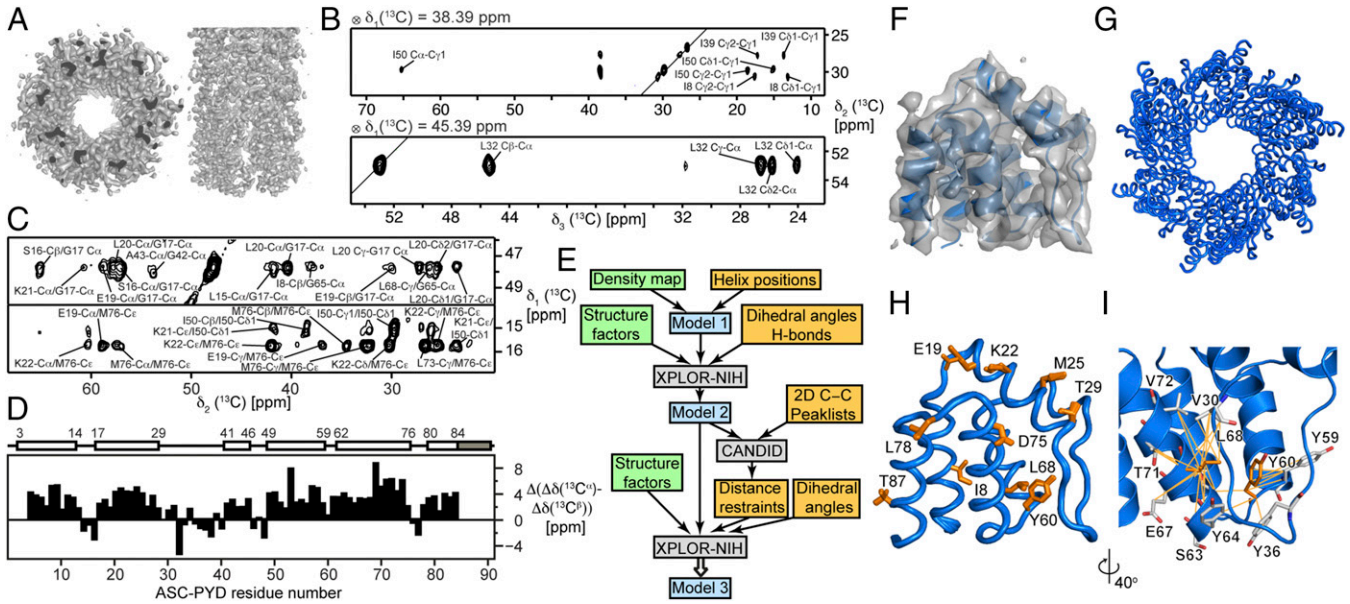

Fig. 2. Structure determination of the ASC-PYD filament by the combination of cryo-EM and solid-state NMR data. (*A*) Electron density map of the ASC-PYD filament obtained by cryo-EM and image processing. Darker segments are the inner bulk volume of the density map. (*B*) Strips from a 3D ^{13}C-correlation spectrum of a [U-^{13}C]-labeled ASC-PYD filament. The strips were taken at the ^{13}Cα positions of residues Ile-50 and Leu-32, respectively. (*C*) Strips from a 2D [^{13}C,^{13}C]-DARR (*Upper*) and a CHHC (*Lower*) spectrum. Pairwise ^{13}C–^{13}C contacts as identified by CANDID are shown using the one-letter amino acid code and residue number. (*D*) Secondary chemical shifts of ASC-PYD in the filament from solid-state NMR experiments. The data identify six α-helices, as indicated above the panel with the starting and ending residue numbers. (*E*) Flowchart of the ab initio structure determination of the ASC-PYD filament. The data contributions from solid-state NMR spectroscopy and cryo-EM are indicated by yellow and green rectangles, respectively. The individual structural models 1–3 are shown in light blue. Software packages are identified in gray rectangles. See *SI Materials and Methods* for details. (*F*) Cryo-EM density reconstruction superimposed with the single-subunit ASC-PYD structure. (*G* and *H*) Backbone superimposition of the 20 lowest-energy conformers of the ASC-PYD filament (*G*) and a single monomer within the assembled filament (*H*). The conformational ensemble of 10 arbitrarily selected side chains is shown as stick models in orange. (*I*) Structural features of a single ASC-PYD monomer as part of the filament. The spectrally ambiguous distance constraints between Tyr60 and Leu68 (orange) and the neighboring residues (gray), obtained from solid-state NMR experiments are shown as orange lines.

better defined in model 3 through the integration of the distance restraints. Therefore, we conclude that the resolution of the EM map was high enough so that, in combination with NMR-derived secondary structure information, a high-resolution structure can be obtained de novo, without the requirement of prior knowledge of the protein monomer structure (model 2). Because this procedure requires only NMR chemical-shift assignments for the protein backbone, this approach is accessible for even larger proteins with contemporary technology (35). Additionally, the fact that CANDID interprets 91% of all observed cross-peaks using the narrow tolerance of 0.2 ppm for ^{13}C chemical shifts is an important cross-validation of models 2 and 3. Finally, the Fourier shell correlation (FSC) between the final structural model and the density map showed a resolution of 4.3 Å (Fig. S2*E*).

Structure of the Mouse ASC-PYD Filament. Mouse ASC-PYD forms a triple-stranded, right-handed helical filament in which each PYD interacts with six adjacent subunits through three asymmetric interfaces, types I–III (Fig. 3 *A*–*F* and Movies S3 and S4). Interface type I is formed by amino acid residues belonging to helices 1 and 4 on one subunit and helix 3 in the adjacent subunit, defining helical PYD strands winding around the helix axis (Fig. 3*D*). It involves interactions between residues of opposite charges that contribute to the filament stabilization. The solvent-exposed positively charged side chains of Lys22, Lys26, and Lys21 from helix 2 and Arg41 from helix 3 are involved in electrostatic interactions with the negatively charged side chain of residues Glu13 and Asp6 from helix 1 and residues Asp48 and Asp54 from helix 4 of the neighboring subunit. In addition, a network of hydrophobic interactions is formed by Leu9, Met25, Val30, and Ile50. The lateral contact of strands parallel to the filament axis emerges from interface type II (Fig. 3*E*). Residues in helices 4 and 5 and in the central part of the loop between helixes 2 and 3 on one subunit interact with residues at the corner of helices 5 and 6 of the next subunit by specific hydrophobic interactions. The interactions of Tyr59 and Tyr60 from the loop between helices 4 and 5 and Gly77 and Leu78 from the loop between helices 5 and 6 of the neighboring subunit define the contact surface between two helical layers. In addition, the contribution of further charged and uncharged side chains suggests a more heterogeneous interaction network. The type III interface is formed by residues from the end of helix 1 and the sequential short loop on one subunit with helix 3 on the adjacent subunit, mediating the contact of a helical strand with an adjacent helical layer (Fig. 3*F*). It is defined by interactions involving both polar and hydrophobic side chains. The charged residues Glu13, Glu19, and Arg41 are located close to this interface but do not form specific salt-bridge interactions.

The Monomer Structure Is Maintained in the Filament. Mouse ASC-PYD is soluble at low pH conditions, leading to well-folded, monomeric species as indicated by the signal dispersion and narrow line widths of the 2D [^{15}N,^{1}H]-heteronuclear single-quantum coherence (HSQC) spectrum (Fig. S4*A*). Analysis of the backbone secondary chemical shifts confirmed the position of the six α-helices at positions 3–14, 17–29, 41–46, 49–59, 62–76, and 80–84 as the secondary structure elements of mouse ASC-PYD in solution. Thus these helices are located at the same positions in the dissolved monomer as in the filament form. Furthermore, a comparison of backbone dihedral angles ϕ and ψ as predicted by TALOS+ (36) from the backbone chemical shifts confirms that all secondary structure elements are equally retained in the solution and filament forms of mouse ASC-PYD, thus explaining the absence of major structural rearrangements upon filament formation. A direct comparison of the backbone chemical shifts of the monomer form of ASC-PYD in solution with the filament form reveals a largely identical conformation, with chemical-shift differences mostly smaller than 0.6 ppm. Notable exceptions can be found; these exceptions point directly to residues located at the subunit interfaces, where slight

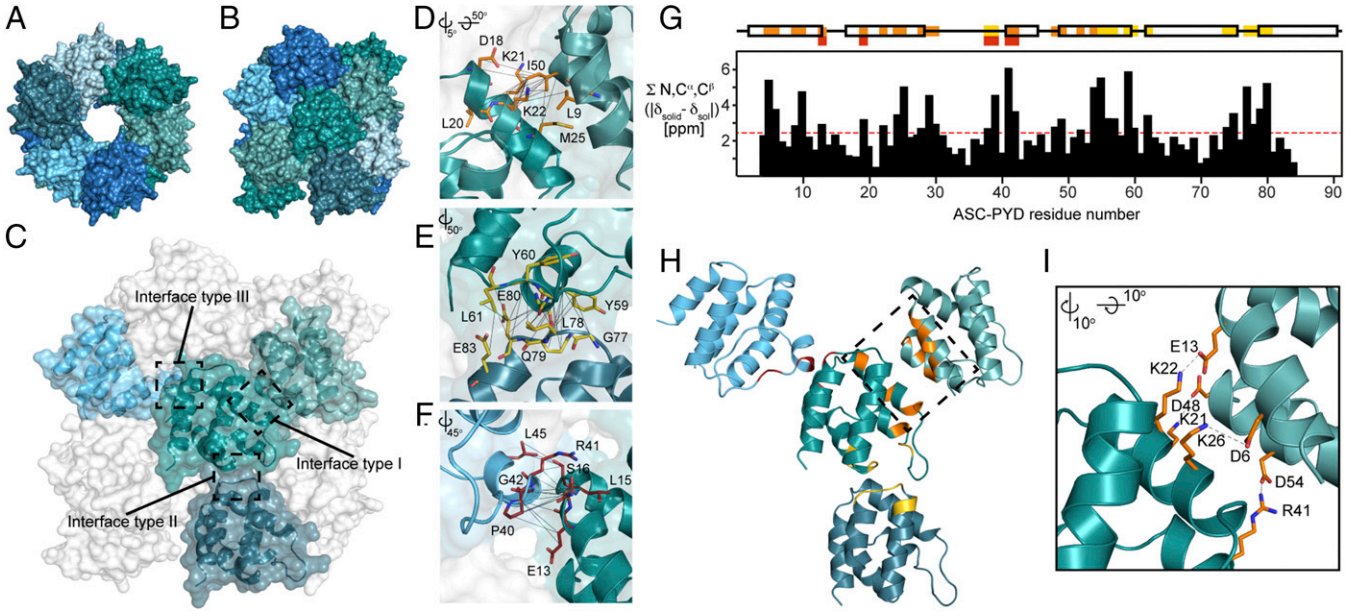

Fig. 3. 3D arrangement of the ASC-PYD filament. (*A* and *B*) Top (*A*) and side (*B*) views of the ASC-PYD filament in surface representation. The three helical oligomer strands are colored blue, teal, and dark blue, and individual ASC-PYD subunits have alternating darker and lighter shades. (*C*) Four ASC-PYD monomers are shown in surface representation as part of the filament using the color code in *A* and *B*. Three interaction interfaces I–III are indicated by dashed square rectangles. (*D*–*F*) Detailed view of interaction interfaces I–III, respectively. Intermolecular atom-pair contacts observed as ambiguous peaks by solid-state NMR spectroscopy and identified by CANDID are indicated by solid black lines. The residues defining interfaces I, II, and III are labeled and colored orange, yellow, and red, respectively. (*G*) Chemical-shift differences between solution- and solid-state chemical shifts for the nucleus ^{15}N, ^{13}Cα, and ^{13}Cβ. Chemical-shift variations larger than the mean value are marked with different color codes on the secondary structure elements. Residues that belong to the type I, II, and III interfaces are marked in orange, yellow, and red, respectively. (*H*) Structural location of the residues with significant chemical-shift differences between the monomeric and filament forms, as identified and using the color code in *G*. (*I*) Structural details of interface type I as indicated by the dashed square rectangle in *H*. Side chains involved in intersubunit salt bridges are shown as stick models and with their sequence labels.

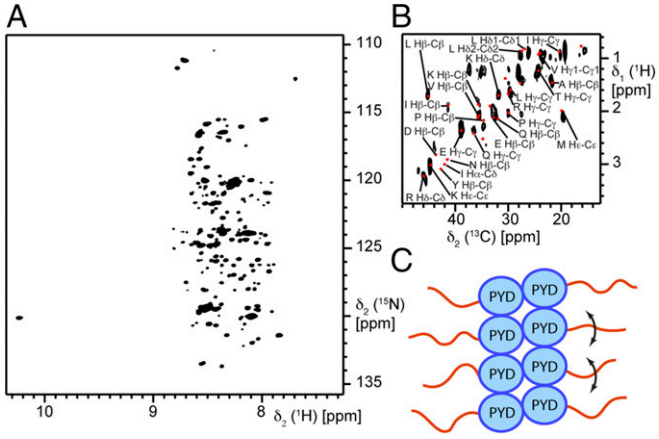

Fig. 4. The CARD in the mouse ASC-FL filament is flexibly unfolded. (*A*) Solid-state 2D [^{15}N,^{1}H]-HSQC spectrum of [U-^{13}C,^{15}N]-labeled ASC-FL. (*B*) Carbon-detected refocused INEPT spectrum of [U-^{13}C,^{15}N]-labeled mouse ASC-FL. Random-coil chemical-shift positions for the 20 common amino acids are reported as red dots. (*C*) Model of the ASC-FL filament. Multiple ASC-PYDs (blue) provide the structural scaffold for the filament formation; the ASC-CARDs (orange) remain flexible relative to the ordered filament core and probably exist in random-coil form.

conformational changes are induced by the packing effects upon filament formation (Fig. 3 *G–I* and Fig. S4*B–E*). Thus these chemical-shift data independently confirm the three asymmetric interfaces that are characteristic of the filament architecture.

Conservation of the ASC-PYD Filament Architecture. A comparison of the mouse ASC-PYD filament structure with the human ASC-PYD filament (PDB ID code 3J63) (16) shows that the spatial assemblies and the structures of the monomer subunits are highly similar (Fig. S5). The structures of monomeric subunits of human and mouse ASC-PYD from the respective filament structures overlay with a backbone rmsd of 1.1 Å. Also the 3D arrangement of the subunits toward the filament structure shows the same overall arrangement (helical parameters: 53° rotation, 14.2-Å rise for mouse versus 52.9° rotation, 13.9-Å rise for human). Although an agreement in the tertiary structure between mouse and human ASC is expected, because they differ in only 20 of the 93 residues, the identity in the quaternary structure is noteworthy. This finding suggests functional conservation of the ASC polymerization mechanism as part of the innate immune response system in mouse, human, and possibly other species.

Dynamics and Flexibility of the CARD. MAS solid-state NMR spectra can be recorded with different polarization-transfer schemes. Experiments based on cross-polarization (CP) techniques filter for rigid parts of the assemblies, whereas INEPT-based experiments monitor flexible parts of the molecular assemblies. Our initial CP-based experiments of ASC-FL filaments have established that the rigid parts of the filament are formed entirely by the PYD and that the CARD is a flexible part of the filament arrangement (Fig. 1). Consequently, INEPT-based experiments (37) were used to obtain spectral information on the conformation and dynamics of this domain. The 2D [^{15}N,^{1}H]-INEPT spectrum of mouse ASC-FL filaments shows a set of ∼105 strong and multiple additional weak backbone amide correlation cross-peaks, with chemical-shift values in the random-coil region and the small dispersion typical of flexible polypeptide chains (Fig. 4*A*). These signals must arise from the 14-residue linker and/or the 89-residue CARD, because a corresponding INEPT spectrum of mouse ASC-PYD filaments did not contain any peaks. Furthermore, the narrow dispersion of amide proton chemical shifts indicates that the linker and probably a major part of or all the CARD populates a conformational ensemble of flexibly unfolded structures in fast equilibrium, similar to a random-coil ensemble. Consistently, 2D INEPT-based [^{1}H,^{13}C]-correlation spectra of the mouse ASC-FL filament also feature no significant chemical-shift dispersion, resulting in the observation of few resonance correlations at the random-coil chemical-shift position (Fig. 4*B*). In our preparations of the mouse ASC filament, the CARD thus is flexible while attached to the well-folded, rigid filament core (Fig. 4*C*).

Robustness of the ASC Inflammasome Architecture. To test the physiological effects of ASC mutations on inflammasome signaling and to avoid overexpression artifacts, we reconstituted immortalized mouse *Asc*$^{-/-}$ macrophages with endogenous levels of WT and mutant versions of N-terminally mCherry-tagged ASC-FL. Based on the mouse ASC-PYD structure and previously reported studies (38), mutations K21A and K26A in interface I were selected (Fig. 5 and Fig. S6). As expected, the induction of cell death and IL-1β secretion upon activation of the PYD-containing inflammasome sensors NLRP3 and absent in melanoma 2 (AIM2) was abrogated by each of these mutations. Consistent with the deficiency in signaling, no ASC specks could be detected in macrophages expressing these two single-amino acid mutants. Furthermore, the induction of cell death upon stimulation of the receptors NLRC4, which is ASC independent (39, 40), is not affected by the K21A and K26A mutations (Fig. S6*D*). However, the mutations significantly reduced IL-1β release and completely abolished ASC speck formation during *Salmonella* infection (Fig. S6*D*). In line with previous reports that show the importance of functional ASC for these aspects of NLRC4 biology (40, 41). These data show that mutations in the type I interface can prevent ASC speck formation and inflammasome signaling during activation of the three best-studied inflammasome receptors, NLRP3, AIM2, and NLRC4. The disruption of filament formation upon mutation of lysine 21 or 26 to alanine confirms the importance of the precise balance of charged residues in interface I and suggests that the mechanism of filament assembly proposed for the in vitro reconstruction is extendable to cell cultures. This finding indicates that, independently of which ligand and receptor induce inflammasome activation, the architecture of the filaments in the ASC speck remains conserved.

Discussion

The integration of solid-state NMR data with a cryo-EM density map used here toward a joint determination of structure is one of

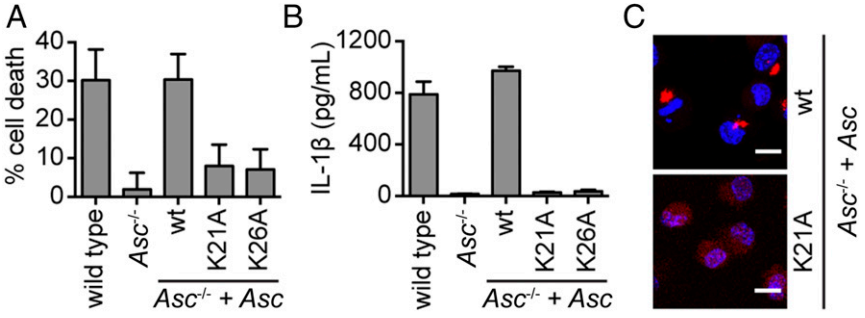

Fig. 5. Effect of single point mutations on ASC-dependent signaling. (*A* and *B*) Cell death as measured by lactate dehydrogenase (LDH) release (*A*) and IL-1β secretion (*B*). (*C*) Overview images showing DNA in blue and ASC in red in LPS-primed immortalized mouse macrophages from the indicated genotypes: wild-type (wt), *Asc*$^{-/-}$, or *Asc*$^{-/-}$ expressing endogenous levels of wild-type (wt) or ASC-mCherry K21A and K26A. Macrophages were stimulated with 5 mM ATP. (Scale bars, 10 μm.)

very few recent examples of this emerging approach. The other published example comprises structural studies of the type III secretion needle, also a helical arrangement (20, 42). Importantly, the two techniques provide complementary information, leading to an overall comprehensive description extending beyond the power and resolution of cryo-EM or solid-state NMR alone. The EM density map in combination with the identification of helix location and the use of individual dihedral backbone angle restraints from solid-state NMR data allow unambiguous determination of the backbone structure de novo. Thereby, the amount of information for solid-state NMR experiments can be increased gradually from backbones to side chains to intermonomer correlations by recording and analyzing additional experiments. This feature allows a convergence of the structure-determination procedure, as demonstrated here in the stepwise protocol from models 1–3. The measurement of NMR distance restraints, considerably more laborious than the determination of backbone angles, was shown to be consistent with, but not necessary for, backbone localization. It did lead to a significant, albeit relatively minor, improvement of side-chain conformations.

The mouse ASC filament is a helical arrangement of individual PYDs mediated by electrostatic and hydrophobic intermolecular contacts along specific interfaces. The comparison with the previously established human ASC-PYD filament (16) shows that the molecular architecture is strongly conserved between the two species. The filament architecture thus is encoded in the amino acid sequence of ASC and determines the correct quaternary assembly upon inflammatory stimulation. This observation suggests that the molecular mechanism of the ASC-dependent innate immune response is conserved and follows the same biophysical principles in both species, implicating a biological role for the filament structure. Thereby, the helical arrangement and the interfaces I–III are in full agreement with other reported helical arrangements of death domains (17, 43). The CARD in ASC-FL filaments was found to be dynamic and at least partially unfolded in our experimental conditions. Low thermodynamic stability of a CARD has been reported before [e.g., in the procaspase-1 CARD (44)], and a population shift toward unfolded conformations upon filament formation might constitute a general functional element of ASC. For example, the dynamic nature of ASC-CARD could be required for the interaction with downstream caspase-1, or it may reduce the amount of CARD–CARD-mediated filament branching and thus control the protein density in the 3D ASC speck in vivo. The structure of mouse ASC filament provides an ideal basis for structure-based mutagenesis, as demonstrated with our single point mutation experiments in cultured macrophages. This approach allows experiments at native expression levels of ASC, avoiding artifactual induction of ASC filament formation.

Materials and Methods

Experimental details of sample preparation, cryo-electron microscopy, NMR spectroscopy and the cell culture experiments are given in *SI Materials and Methods*.

ACKNOWLEDGMENTS. We thank Vesna Oliveri, Janine Zankl, and Timm Maier for experimental help and discussions. This work was supported by NIH Grant EB001567 (to E.H.E.), by Swiss National Science Foundation (SNSF) Grants 200020_146757 (to B.H.M.), ANR-12-BS08-0013-01 (to A.B.), and ANR-11-BSV8-021-01 (to A.B.), and by the Swiss Initiative in Systems Biology SystemsX.ch (Research, Technology and Development Project Cellular Imaging and Nanoanalytics).

1. Franchi L, Muñoz-Planillo R, Núñez G (2012) Sensing and reacting to microbes through the inflammasomes. *Nat Immunol* 13(4):325–332.
2. Lamkanfi M, Dixit VM (2014) Mechanisms and functions of inflammasomes. *Cell* 157(5):1013–1022.
3. Vanaja SK, Rathinam VA, Fitzgerald KA (2015) Mechanisms of inflammasome activation: Recent advances and novel insights. *Trends Cell Biol* 25(5):308–315.
4. Schroder K, Tschopp J (2010) The inflammasomes. *Cell* 140(6):821–832.
5. Walsh JG, Muruve DA, Power C (2014) Inflammasomes in the CNS. *Nat Rev Neurosci* 15(2):84–97.
6. Strowig T, Henao-Mejia J, Elinav E, Flavell R (2012) Inflammasomes in health and disease. *Nature* 481(7381):278–286.
7. Lamkanfi M, Dixit VM (2012) Inflammasomes and their roles in health and disease. *Annu Rev Cell Dev Biol* 28:137–161.
8. Hu Z, et al. (2013) Crystal structure of NLRC4 reveals its autoinhibition mechanism. *Science* 341(6142):172–175.
9. Lu A, Wu H (2015) Structural mechanisms of inflammasome assembly. *FEBS J* 282(3):435–444.
10. Masumoto J, et al. (1999) ASC, a novel 22-kDa protein, aggregates during apoptosis of human promyelocytic leukemia HL-60 cells. *J Biol Chem* 274(48):33835–33838.
11. Srimathi T, et al. (2008) Mapping of POP1-binding site on pyrin domain of ASC. *J Biol Chem* 283(22):15390–15398.
12. Hiller S, et al. (2003) NMR structure of the apoptosis- and inflammation-related NALP1 pyrin domain. *Structure* 11(10):1199–1205.
13. Vajjhala PR, et al. (2014) Identification of multifaceted binding modes for pyrin and ASC pyrin domains gives insights into pyrin inflammasome assembly. *J Biol Chem* 289(34):23504–23519.
14. de Alba E (2009) Structure and interdomain dynamics of apoptosis-associated speck-like protein containing a CARD (ASC). *J Biol Chem* 284(47):32932–32941.
15. Liepinsh E, et al. (2003) The death-domain fold of the ASC PYRIN domain, presenting a basis for PYRIN/PYRIN recognition. *J Mol Biol* 332(5):1155–1163.
16. Lu A, et al. (2014) Unified polymerization mechanism for the assembly of ASC-dependent inflammasomes. *Cell* 156(6):1193–1206.
17. Qiao Q, et al. (2013) Structural architecture of the CARMA1/Bcl10/MALT1 signalosome: Nucleation-induced filamentous assembly. *Mol Cell* 51(6):766–779.
18. Park HH, et al. (2007) Death domain assembly mechanism revealed by crystal structure of the oligomeric PIDDosome core complex. *Cell* 128(3):533–546.
19. Wasmer C, et al. (2008) Amyloid fibrils of the HET-s(218-289) prion form a beta solenoid with a triangular hydrophobic core. *Science* 319(5869):1523–1526.
20. Loquet A, et al. (2012) Atomic model of the type III secretion system needle. *Nature* 486(7402):276–279.
21. Debelouchina GT, Platt GW, Bayro MJ, Radford SE, Griffin RG (2010) Intermolecular alignment in β2-microglobulin amyloid fibrils. *J Am Chem Soc* 132(48):17077–17079.
22. Petkova AT, et al. (2002) A structural model for Alzheimer's beta -amyloid fibrils based on experimental constraints from solid state NMR. *Proc Natl Acad Sci USA* 99(26):16742–16747.
23. Meier BH, Böckmann A (2015) The structure of fibrils from 'misfolded' proteins. *Curr Opin Struct Biol* 30:43–49.
24. Lu JX, et al. (2013) Molecular structure of β-amyloid fibrils in Alzheimer's disease brain tissue. *Cell* 154(6):1257–1268.
25. Scherer S, et al. (2014) 2dx_automator: Implementation of a semiautomatic high-throughput high-resolution cryo-electron crystallography pipeline. *J Struct Biol* 186(2):302–307.
26. Li X, et al. (2013) Electron counting and beam-induced motion correction enable near-atomic-resolution single-particle cryo-EM. *Nat Methods* 10(6):584–590.
27. Egelman EH (2000) A robust algorithm for the reconstruction of helical filaments using single-particle methods. *Ultramicroscopy* 85(4):225–234.
28. Schuetz A, et al. (2010) Protocols for the sequential solid-state NMR spectroscopic assignment of a uniformly labeled 25 kDa protein: HET-s(1-227). *ChemBioChem* 11(11):1543–1551.
29. Ravotti F, et al. (September 24, 2015) Sequence-specific solid-state NMR assignments of the mouse ASC PYRIN domain in its filament form. *Biomol NMR Assign*, 10.1007/s12104-015-9647-6.
30. Igumenova TI, et al. (2004) Assignments of carbon NMR resonances for microcrystalline ubiquitin. *J Am Chem Soc* 126(21):6720–6727.
31. Emsley P, Cowtan K (2004) Coot: Model-building tools for molecular graphics. *Acta Crystallogr D Biol Crystallogr* 60(Pt 12 Pt 1):2126–2132.
32. Schwieters CD, Kuszewski JJ, Tjandra N, Clore GM (2003) The Xplor-NIH NMR molecular structure determination package. *J Magn Reson* 160(1):65–73.
33. Kneller DG, Kuntz ID (1993) UCSF Sparky – an NMR display, annotation and assignment tool. *J Cell Biochem* 53(S17C):254–254.
34. Herrmann T, Güntert P, Wüthrich K (2002) Protein NMR structure determination with automated NOE assignment using the new software CANDID and the torsion angle dynamics algorithm DYANA. *J Mol Biol* 319(1):209–227.
35. Habenstein B, et al. (2011) Extensive de novo solid-state NMR assignments of the 33 kDa C-terminal domain of the Ure2 prion. *J Biomol NMR* 51(3):235–243.
36. Shen Y, Delaglio F, Cornilescu G, Bax A (2009) TALOS+: A hybrid method for predicting protein backbone torsion angles from NMR chemical shifts. *J Biomol NMR* 44(4):213–223.
37. Morris GA, Freeman R (1979) Enhancement of nuclear magnetic resonance signals by polarization transfer. *J Am Chem Soc* 101(3):760–762.
38. Moriya M, et al. (2005) Role of charged and hydrophobic residues in the oligomerization of the PYRIN domain of ASC. *Biochemistry* 44(2):575–583.
39. Mariathasan S, Monack DM (2007) Inflammasome adaptors and sensors: Intracellular regulators of infection and inflammation. *Nat Rev Immunol* 7(1):31–40.
40. Broz P, von Moltke J, Jones JW, Vance RE, Monack DM (2010) Differential requirement for Caspase-1 autoproteolysis in pathogen-induced cell death and cytokine processing. *Cell Host Microbe* 8(6):471–483.
41. Van Opdenbosch N, et al. (2014) Activation of the NLRP1b inflammasome independently of ASC-mediated caspase-1 autoproteolysis and speck formation. *Nat Commun* 5:3209.
42. Demers JP, et al. (2014) High-resolution structure of the Shigella type-III secretion needle by solid-state NMR and cryo-electron microscopy. *Nat Commun* 5:4976.
43. Lin SC, Lo YC, Wu H (2010) Helical assembly in the MyD88-IRAK4-IRAK2 complex in TLR/IL-1R signalling. *Nature* 465(7300):885–890.
44. Chen YR, Clark AC (2004) Kinetic traps in the folding/unfolding of procaspase-1 CARD domain. *Protein Sci* 13(8):2196–2206.
45. Güntert P, Dötsch V, Wider G, Wüthrich K (1992) Processing of multi-dimensional NMR data with the new software PROSA. *J Biomol NMR* 2(6):619–629.